Article

SnS$_2$ Nanosheets with RGO Modification as High-Performance Anode Materials for Na-Ion and K-Ion Batteries

Leqiang Wu, Hengjia Shao, Chen Yang, Xiangmin Feng, Linxuan Han, Yanli Zhou, Wei Du [ID]**, Xueqin Sun, Zhijun Xu, Xiaoyu Zhang** [ID]**, Fuyi Jiang ***[ID]** and Caifu Dong ***

School of Environmental and Material Engineering, Yantai University, Yantai 264005, China;
wlq_246@163.com (L.W.); shao0331@163.com (H.S.); yc083625@163.com (C.Y.); fxm18763285297@163.com (X.F.);
a13156280283@163.com (L.H.); zhouyanli@ytu.edu.cn (Y.Z.); duwei@ytu.edu.cn (W.D.); sxq@ytu.edu.cn (X.S.);
xuzhijun@ytu.edu.cn (Z.X.); zhangxiaoyu@ytu.edu.cn (X.Z.)
* Correspondence: fyjiang@ytu.edu.cn (F.J.); dongcf@ytu.edu.cn (C.D.)

Abstract: To date, the fabrication of advanced anode materials that can accommodate both Na$^+$ and K$^+$ storage is still very challenging. Herein, we developed a facile solvothermal and subsequent annealing process to synthesize SnS$_2$/RGO composite, in which SnS$_2$ nanosheets are bonded on RGO, and investigated their potential as anodes for Na$^+$ and K$^+$ storage. When used as an anode in SIBs, the as-prepared SnS$_2$/RGO displays preeminent performance (581 mAh g^{-1} at 0.5 A g^{-1} after 80 cycles), which is a significant improvement compared with pure SnS$_2$. More encouragingly, SnS$_2$/RGO also exhibits good cycling stability (130 mAh g^{-1} at 0.3 A g^{-1} after 300 cycles) and excellent rate capability (520.8 mAh g^{-1} at 0.05 A g^{-1} and 281.4 mAh g^{-1} at 0.5 A g^{-1}) when used as anode for PIBs. The well-engineered structure not only guarantees the fast electrode reaction kinetics, but also ensures superior pseudocapacitance contribution during repeated cycles, which has been proved by kinetic analysis.

Keywords: SnS$_2$; anode; sodium-ion batteries; potassium-ion batteries

1. Introduction

With the intensification of environmental pollution, green renewable energy has currently become an active area of research [1,2]. Among numerous energy storage devices, sodium-ion batteries (SIBs) and potassium-ion batteries (PIBs) have gained extensive concern for energy storage because of their similar energy storage mechanisms to lithium-ion batteries (LIBs) and the abundant sodium and potassium resources [3–5]. However, the low capacity of commercial graphite anodes for Na-ion and K-ion storage has greatly limited the large-scale development of SIBs and PIBs [6–8]. Therefore, it is imperative to develop high-performance anode materials for both SIBs and PIBs.

Specifically, the hexagonal tin (IV) sulfide (SnS$_2$) possesses unique two-dimensional (2D) layered structure with large interlayer spacing and high specific capacity based on both conversion and alloying processes [9–11], which makes it more appropriate for Na-ion and K-ion storage. Unfortunately, similar to other TMSs, SnS$_2$ also has the low intrinsic conductivity and the dramatic volume and structural changes, which will easily lead to the poor sluggish kinetics and rapid capacity reduction in the process of Na$^+$ and K$^+$ insertion/extraction [12–15]. The construction of SnS$_2$ and various conductive carbona-ceous composite has become one of the most effective approaches to ameliorate these problems [16–18]. For instance, the carbon-coated SnS$_2$ nanosheet composite fabricated by Li et al., delivered a reversible capacity of ~420 mAh g^{-1} at a current density of 500 mA g^{-1} after 100 cycles for Na$^+$ storage [19]. SnS$_2$ and rGO composite synthesized by Glushenkov, displayed a reversible capacity of 250 mAh g^{-1} at 25 mA g^{-1} after 30 cycles for PIBs [20]. Even though the cycling stability has been improved via carbon modified anode materi-

als, how to achieve higher-performance SnS_2 electrode with long cycle life is still a huge challenge for SnS_2.

Herein, SnS_2/RGO nanoarrays have been fabricated via a facile solvothermal method along with a subsequent annealing process. GO is chosen as the substrate because the rich functional groups on GO can increase the nucleation sites with metal ions, which contributes to form a strong and close-coupled interface between RGO and SnS_2. Benefiting from the unique structural characteristics, SnS_2/RGO displays higher cycle stability and better rate capability than the pristine SnS_2. For example, the prepared SnS_2/RGO shows a high reversible capacity of 653.8 mAh g^{-1} at 100 mA g^{-1}, and outstanding rate performance (593 mAh g^{-1} at 200 mA g^{-1} and 400 mAh g^{-1} at 2000 mA g^{-1}) for SIBs. Moreover, SnS_2/RGO also displays a high-rate capacity (520.8 mAh g^{-1} at 50 mA g^{-1} and 281.4 mAh g^{-1} at 500 mA g^{-1}) and good cycling stability (130 mAh g^{-1} at 300 mA g^{-1} after 300 cycles) for K-ion storage. The fast electrode reaction kinetics and superior pseudo-capacitance contribution may be the reason for the excellent performance, which has been proved by kinetic analysis. Thus, the present study provides a novel strategy to prepare SnS_2 and rGO composite with excellent performance for both sodium and potassium storage and this strategy which may be extended to fabricate other high-performance electrode materials for energy storage.

2. Materials and Methods

2.1. Synthesis of SnS_2, and SnS_2/RGO Nanoarrays

In a typical preparation, 10 mg GO (prepared by the modified Hummers method) was first dispersed in 8 mL isopropanol. Then 0.172 mmol (38.8 mg) $SnCl_2 \cdot 2H_2O$ and 0.761 mmol (62.4 mg) 2-methylimidazole (2-MIN) were added into the above solution and stirred vigorously for 12 h at 25 °C. After that, 0.8 mmol (60 mg) thioacetamide (TAA) was added into the solution under stirring. After stirring for another 2 h, the solution was transferred into a Teflon-lined autoclave (25 mL) and kept at 120 °C for 24 h. The solid product was collected and dried. Finally, the precursor annealed at 350 °C with a heating rate of 2 °C min^{-1} in Ar gas for 1 h to gain the final products of SnS_2/RGO. The SnS_2 was produced by similar route, but with no added organic molecules and GO in the solvothermal process.

2.2. Materials Characterization

The morphologies of SnS_2/RGO and SnS_2 were tested by a transmission electron microscope (JEOL-1400 Plus, Tokyo, Japan), the high-resolution TEM (HRTEM JEOL-2011, Tokyo, Japan) and a field emission scanning electron microscope (FESEM, ZEISS Geminisem 300, Oberkochen, Germany). The components of SnS_2/RGO and SnS_2 were analyzed by energy dispersive spectrometry (EDS). Crystallographic phases of SnS_2/RGO and SnS_2 were measured by powder X-ray diffraction (XRD Bruker, D_8-Advanced, Tokyo, Japan) using a Cu Kα radiation. Raman spectroscopy (LabRAM HR 800, Paris, France) with 532 nm laser excitation. X-ray photoelectron spectroscopic (XPS) surveys were performed on an X-ray photoelectron spectrometer (Thermo Scientific Escalab 250Xi, New York, NY, USA), which uses an Al Kα as the excitation source.

2.3. Electrochemical Measurements

For the Na-ion half cells, 2032 coin-type cells were employed. The electrodes were obtained by applying a slurry mixture consisting of active materials (70 wt.%), Super-P (20 wt.%), and polyvinylidene difluoride (PVDF, 10 wt.%), to a copper foil and drying it under vacuum at 60 °C for 6 h. The loading of the active material on each disc was about 1.05–1.4 mg cm^{-2}. A sodium foil with a diameter of about 14 mm was prepared in a glove box under the protection of high-purity argon as a counter electrode using sodium block (Aladdin, 99.7%). The glass fiber (Whatman) was used as the separator and 1 M $NaPF_6$ dissolved in the diethyleneglycoldimethylether acted as electrolyte. To study the electrode performance of SnS_2/RGO for PIBs, CR 2016 coin batteries was built using SnS_2/RGO

as anode, potassium metal was used as counter electrodes. The electrolyte was 3.0 M potassium bis(fluorosulfonyl)imide (KFSI) in TGM. The anode was prepared by casting slurries of active material, super P and PVDF binder in a mass proportion of 7:2:1 onto copper foil with an active material loading of around 1.05–1.4 mg cm^{-2}. The galvanostatic charge/discharge tests were conducted on battery test station (LAND CT-2001A, Wuhan, China) from 0.01–3.0 V. Cyclic voltammetry (CV) tests (0.01–3.0 V) were carried on the CHI 760E electrochemical workstation.

3. Results and Discussion

Figure 1 schematically illustrates the fabrication route of SnS$_2$/RGO and SnS$_2$. The Sn-based nanosheets in-situ grown on graphene oxide (GO) substrate can be obtained via solvothermal reaction by added 2-methylimidazole (2-MIN) and GO substrate in the first step. In the absence of 2-MIN and GO substrate, flower-like three-dimensional microspheres consisting of larger nanosheets are obtained. After a calcination process under Ar atmosphere, SnS$_2$/RGO and SnS$_2$ are obtained.
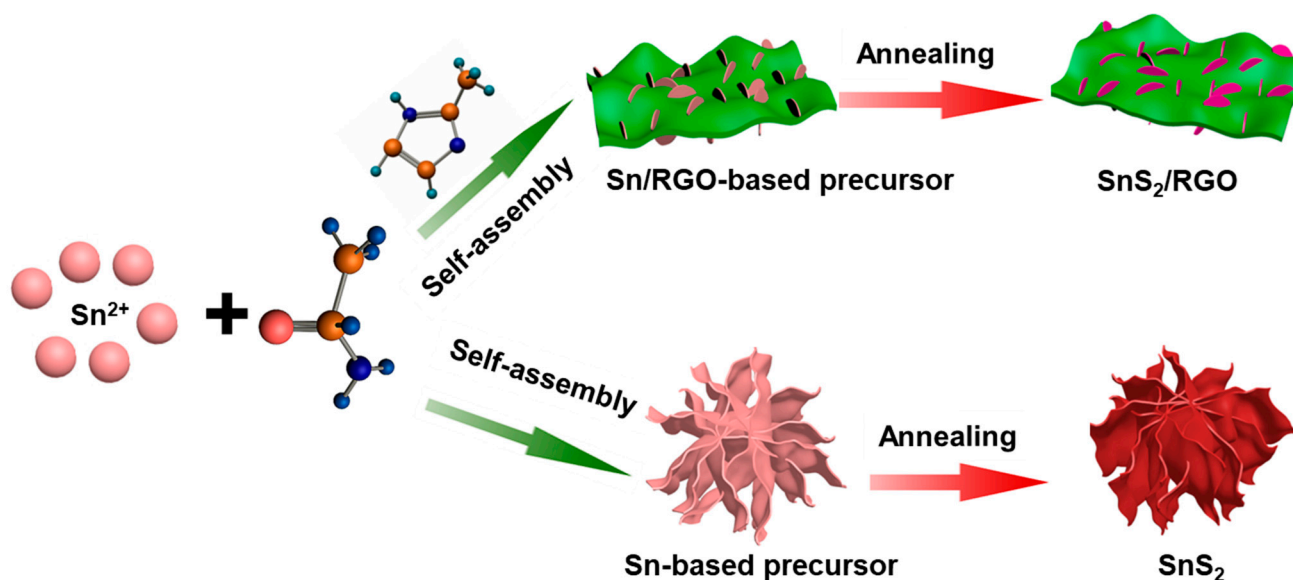

Figure 1. Schematic illustration of the formation process of pure SnS$_2$, and SnS$_2$/RGO.

The FESEM and TEM are carried out to investigate the morphological features of as-prepared materials. Figure 2a and Figure S1 show the detailed morphological character-istics of the precursors. As seen in Figure 2a, the vertical tin-based precursor nanosheets are densely and uniformly grown on both sides of the GO substrate, forming a sandwich-like hierarchical structure. To find out the function of 2-MIN, we performed several comparative experiments by varying the reaction conditions (Figure S1). In the absence of 2-MIN, the same synthesis process produced bare GO sheets and parts of the nanosheets are assembled separately to form a flower-like structure (Figure S1a). In the presence of 2-MIN but without GO, the results showed that the nanosheets are grown on the solid spheres (Figure S1b). In the absence of 2-MIN and GO substrates, the Sn-based precursor shows flower-like three-dimensional spherical structure assembled by larger nanosheets compared with those in the presence of 2-MIN (Figure S1c). The results show that 2-MIN can control the size of precursor nanosheets and induce the growth of nanosheets on GO substrates, which helps to synthesize some novel nanomaterials. FESEM images at different magnifications (Figure 2b,c) show that the nanosheet structure is well retained after annealing at 350 °C. TEM image in Figure 2d further indicates that SnS$_2$ nanosheet is tightly grown on microns GO nanosheets, indicating the synthesized sandwich structure integrates the features of micro- and nanostructures. Figure 2e displays a typical high-resolution transmission elec-tron microscopy (HR-TEM) image of SnS$_2$/RGO, the d-spacing of 0.338 nm corresponding

to the (100) plane in SnS$_2$. Moreover, the selected-area electron diffraction (SAED) pattern (Figure 2f) shows the tagged diffraction rings can be well indexed to (100), (101), (110) and (111) crystal planes of SnS$_2$, respectively. The FESEM image and the corresponding Energy dispersive X-ray spectroscopy (EDX) elemental mapping images of SnS$_2$/RGO are shown in Figure 2g, revealing the homogeneous dispersion of Sn, S, and C throughout the composites, further verifying the nanosheets are well dispersed on the GO substrate throughout the whole network. As shown in Figure S2a, pure Sn-based precursor can also keep the flower structure after annealing. Moreover, the EDS mapping result shown in Figure S2b displays the homogeneous distribution of Sn and S elements throughout the flower-like SnS$_2$ sphere.
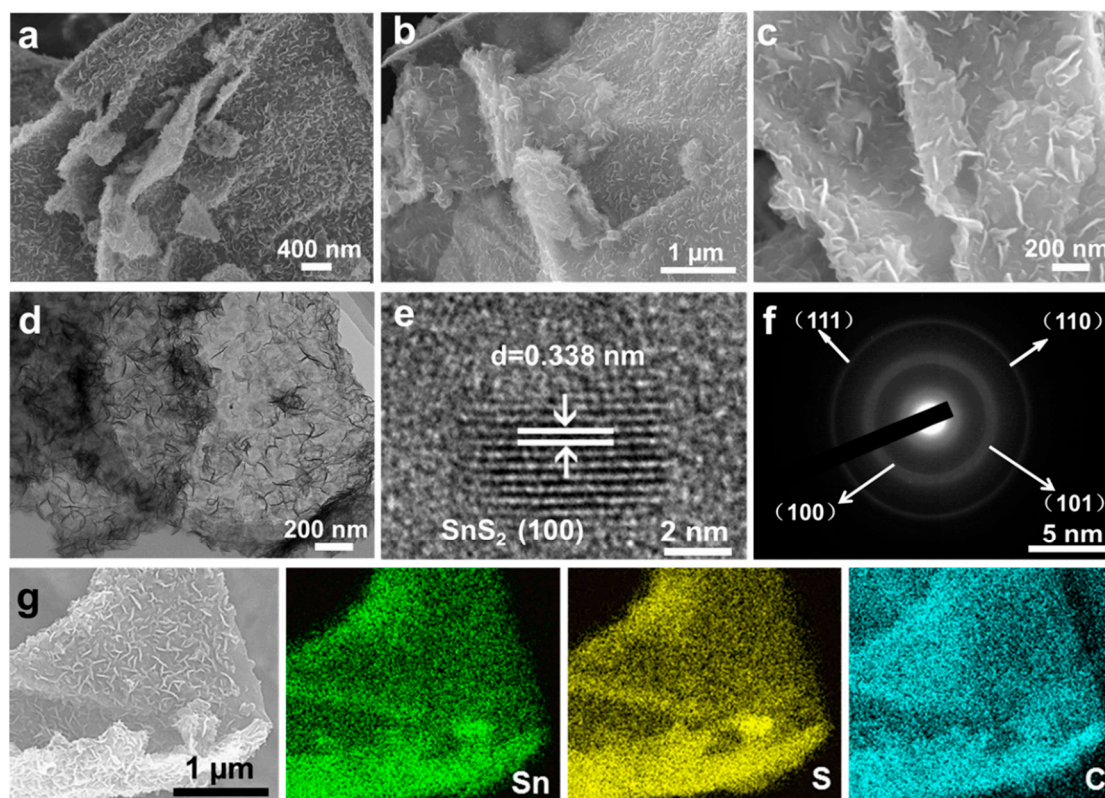

Figure 2. (**a**) FESEM image of Sn/RGO-based precursor. (**b**,**c**) FESEM images of SnS$_2$/RGO at different magnifications. (**d**) TEM image of SnS$_2$/RGO. (**e**) HRTEM image of SnS$_2$/RGO. (**f**) Corresponding SAED pattern. (**g**) A typical FESEM image of SnS$_2$/RGO and the corresponding elemental mappings of Sn, S and C elements (as labeled).

The composition of two samples is investigated by X-ray diffraction (XRD). It can be seen that SnS$_2$/RGO and SnS$_2$ show similar diffraction peaks (Figure 3a) and the diffraction peaks can be attributed to hexagonal SnS$_2$ with P-3m 1 (164) space group (JCPDS no. 23-0677), corresponding to the above mentioned HRTEM and SAED results. There are no obvious diffraction peaks for the carbon phase due to its poor crystallinity. Figure 3b shows a typical 2D layered crystal structure of SnS$_2$, with an interlayer spacing of 0.59 nm. The Raman spectra of SnS$_2$/RGO and GO are shown in Figure 3c. It can be seen that SnS$_2$/RGO and GO have distinct characteristic peaks at ~1344 and 1602 cm^{-1}, which can be attributed to the D (disordered carbon) and G (graphitic carbon) bands of graphite. Moreover, the intensity ratio of D-band to G-band (I_D/I_G) is 1.06, 1.37 for GO, and SnS$_2$/RGO, respectively, indicating more defects in SnS$_2$/RGO [21,22]. In addition, SnS$_2$/RGO exhibits a peak located at 313 cm^{-1}, which corresponds to the A$_{1g}$ vibration of SnS$_2$ [23,24]. Figure S3 presents the N$_2$ adsorption-desorption isotherm profiling of SnS$_2$/RGO. The relatively large surface area (33.885 m^2 g^{-1}) and abundant pores (0.159 cm^3 g^{-1}) of SnS$_2$/RGO can provide adequate active sites and promotes the rapid transport of electron and ions.

X-ray photoelectron spectroscopy (XPS) was further carried out to investigate the surface electronic states and the chemical compositions of SnS_2/RGO. The characteristic peaks of Sn 3d, S 2p, C 1s, and O 1s are observed in the wide survey spectrum (Figure S4). Figure 3d shows the Sn 3d spectrum, in which two strong peaks at 486.1 and 494.5 eV correspond to Sn $3d_{5/2}$ and Sn $3d_{3/2}$ of Sn^{4+} in SnS_2/RGO [25,26]. The high-resolution S spectrum can be convoluted into two peaks at 162.4 eV and 161.3 eV, corresponding to S $2p_{3/2}$ and S $2p_{1/2}$ of S^{2-} (Figure 3e), which further confirms the formation of SnS_2 [27,28]. As presented in Figure 3f, the C 1s spectrum can be divided into two peaks and assigned to the C-C (284.8 eV) and C-O (286.5 eV) bonds, respectively [29,30].
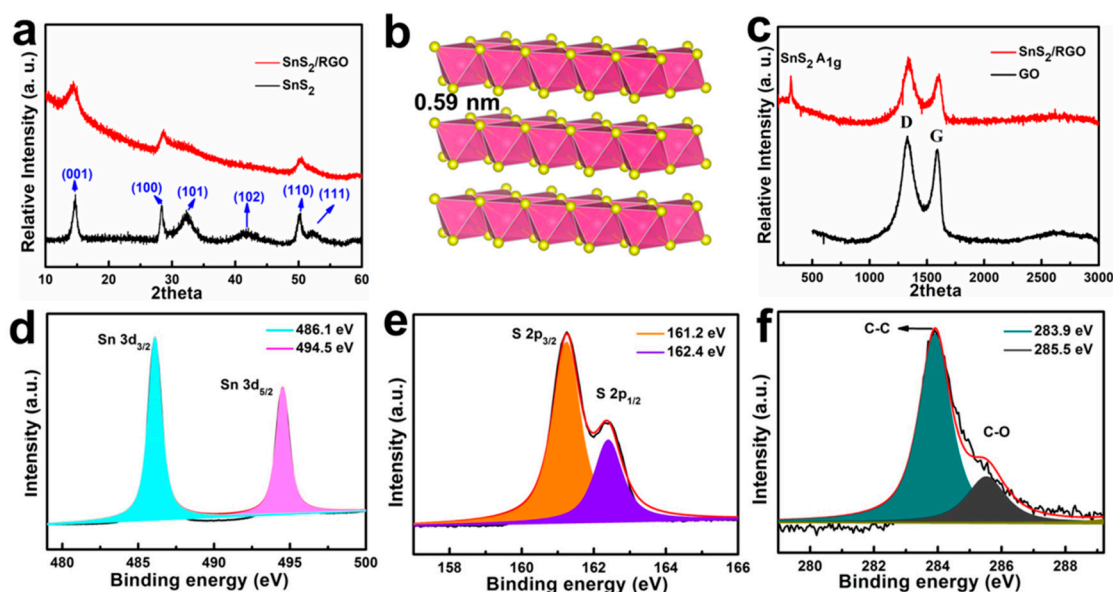

Figure 3. (a) XRD patterns of the obtained SnS_2/RGO and SnS_2. (b) Crystal structure of SnS_2. (c) Raman spectra of SnS_2/RGO and GO. The high-resolution XPS spectra of Sn 3d (d), S 2p (e), and (f) C 1s of SnS_2/RGO.

Inspired by their special structure, the electrochemical performance of the obtained SnS_2/RGO and SnS_2 for SIBs anodes was tested. Figure 4a,b display the galvanostatic charge-discharge (GCD) curves of SnS_2/RGO and SnS_2 at 0.1 A g^{-1}, respectively. It can be clearly seen that SnS_2/RGO reveals the better performance than pure SnS_2. For SnS_2/RGO electrode, the discharge and charge capacities of the first cycle are 795.4 and 653.8 mAh g^{-1}, respectively. The initial loss of irreversible capacity is mainly attributable to the irreversible process of electrolyte decomposition and the generation of solid-electrolyte interface (SEI) layers on the electrode surface, which was a common phenomenon in tin-based sulfide anode materials [31,32]. After the initial cycle, the GCD curves are almost repeated in the flowing cycles, which is coinciding with the CV results (Figure S5a), indicating the good stability of SnS_2/RGO electrode. For further comparison, the cycling performance of SnS_2/RGO and SnS_2 was measured at 0.5 A g^{-1} and shown in Figure 4c. SnS_2/RGO displays the better performance than pure SnS_2 electrode and maintains a high capacity of 581 mAh g^{-1} after 80 cycles. The SnS_2/RGO exhibits excellent sodium storage performance that exceeds many previously reported anode materials for SIBs (Table S1). Beside the cycling performance, the SnS_2/RGO electrode also showed excellent rate performance (Figure 4d). It can show specific capacities of 593, 490.5, 425.2, 431.8, 428.1 and 400 mAh g^{-1} at 0.2, 0.4, 0.6, 0.8, 1 and 2 A g^{-1}, respectively. When the current was switched back to 0.2 A g^{-1}, the specific capacity of 491.3 mAh g^{-1} can be regained, which indicated that the SnS_2/RGO electrode has good structural stability. To verify the excellent rate performance of SnS_2/RGO, the morphology of SnS_2/RGO electrode for SIBs after rate performance was observed by FEEM. It can be seen from Figure S5b that the SnS_2 nanosheets become nanoparticles, but still in close contact with graphene, which is an essential aspect for the good rate performance of the material. To further understand the improved electrochemical

performance of SnS_2/RGO electrode, the EIS spectra of the SnS_2/RGO and SnS_2 electrodes are measured before and after 10 cycles. As shown in Figure 4e, SnS_2/RGO shows a much smaller charge transfer impedance (Rct) than pure SnS_2 after 10 cycles at 0.2 A g^{-1}, indicating that the improvement of conductivity benefiting from the introduction of RGO. Moreover, the Warburg coefficient of SnS_2/RGO is 46.6 Ω s$^{-0.5}$ (Figure 4f), which is much smaller than that of SnS_2 (316.1 Ω s$^{-0.5}$), showing that Na-ion has a faster diffusion ability in SnS_2/RGO. These results are coincident with their sodium storage performance.
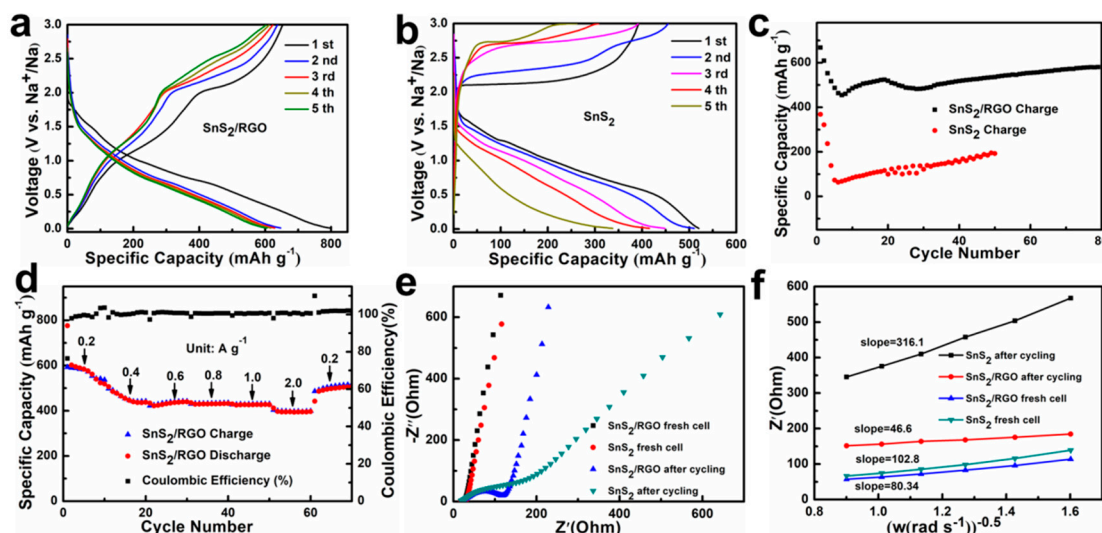

Figure 4. (**a**,**b**) Discharge/charge curves of SnS_2/RGO and SnS_2 at 0.1 A g^{-1}. (**c**) The cycling performance of SnS_2/RGO and SnS_2 at 0.5 A g^{-1}. (**d**) Rate capability at different current densities (0.2–2 A g^{-1}). (**e**) The electrochemical impedance spectra of the SnS_2/RGO and SnS_2 were obtained before and after 10 cycles at 0.2 A g^{-1}. (**f**) The relationship between the Z_{re} and $\omega^{-1/2}$ in the low frequency of SnS_2/RGO and SnS_2.

To better understand the superior capability of SnS_2/RGO, the charge storage behavior and reaction kinetics of SnS_2/RGO and SnS_2 are further analyzed according to CV and GITT tests. Figure 5a and Figure S5c show the CV curves of SnS_2/RGO and SnS_2 at multiple scan rates from 0.1 to 0.6 mV s^{-1}. It should be pointed out that the curves keep its shape even at a high scan rate of 0.6 mV s^{-1}. The dependency between the peak current (i) and the sweep rate (v) is based on Equation (1):

$$i = \alpha v^b,\qquad(1)$$

where b reflects the charge storage behavior [33–35]. Figure 5b and Figure S5d show the b-values of the two redox peaks for SnS_2/RGO and SnS_2, respectively. It can be seen that SnS_2/RGO electrode shows a larger b-values than SnS_2 electrode, indicating the pseudocapacitive contribution ratio of SnS_2/RGO is larger than that of the SnS_2 electrode. The ratios of capacitive contribution can be evaluated by Equation (2) [36–38]:

$$i(v) = k_1 v + k_2 v^{1/2}\qquad(2)$$

where the $k_{1(V)}v$ and the $k_{2(V)}v^{1/2}$ stand for the capacitive-controlled contribution and the diffusion-controlled contribution, respectively. Figure 5c and Figure S5e show the typical CV profiles of the Na-ion capacitive (dark red region) in comparison with the total measured current for SnS_2/RGO and SnS_2 at the scan speed of 0.6 mV s^{-1}. The capacitive-controlled contribution is calculated to be 83.16% of the total Na$^+$ storage at 0.6 mV s^{-1} in SnS_2/RGO, which is higher than that in the case of SnS_2 (74.13%). In addition, the ratios of pseudocapacitive contribution are all increased as the scan rate increases but from 62.76 to 83.16% for SnS_2/RGO, 44.56 to 74.13% for SnS_2 (Figure 5d). Therefore, the improvement of the rate capability may be related to the enhanced contribution ratios of the capacitive behaviors. After that, the galvanostatic intermittent titration technique

(GITT) was carried out to further evaluate the Na^+ solid-state diffusion dynamics of SnS_2/RGO and SnS_2 [39]. The GITT test was performed on at 0.1 A g^{-1} in a voltage range of 0.01–3 V (Figure 5e). Figure S6 shows the detailed test and calculation method. As shown in Figure 5f–i, SnS_2/RGO shows lower reaction resistance and higher D values during the entire cycle than that with SnS_2, which can be probably responsible for the superb performance.
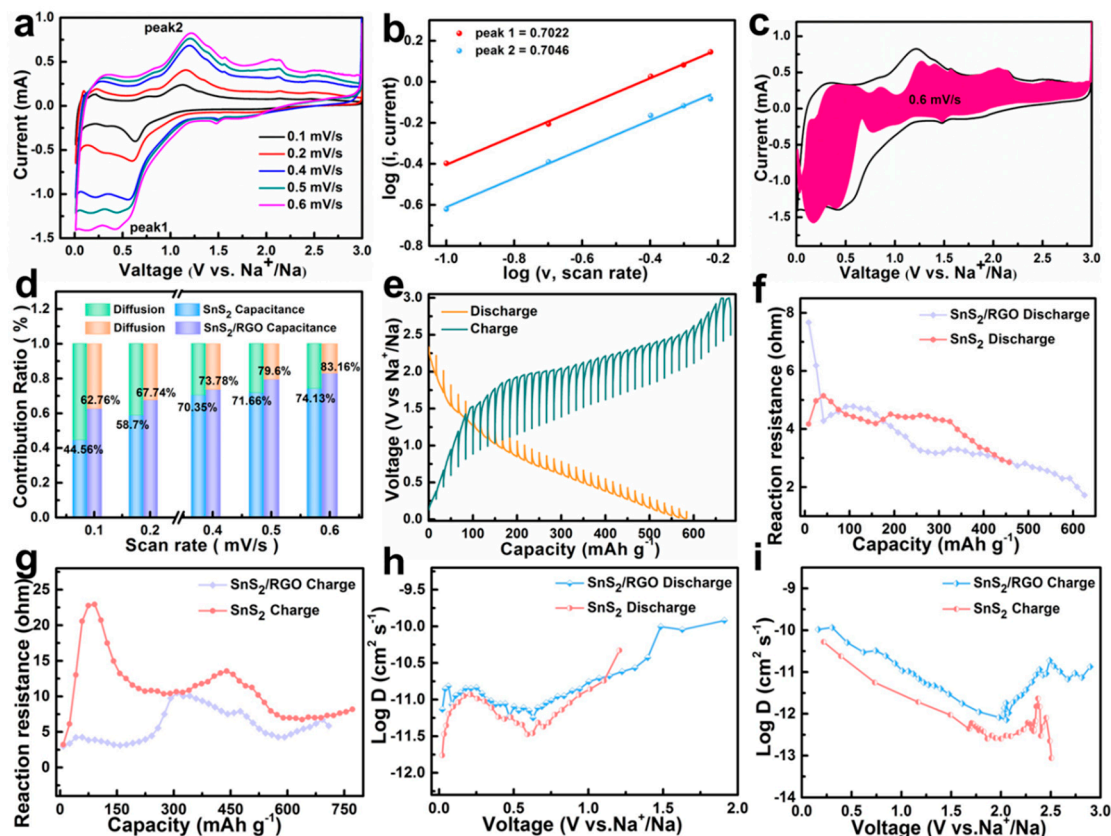

Figure 5. (**a**) CV profiles of SnS_2/RGO at different sweep rates. (**b**) Linear relationship of log (**i**) vs. log (v) plots at each redox peak. (**c**) CV curve with capacitive and diffusion-controlled contributions at 0.6 mV s^{-1}, in which the pseudocapacitive fraction is shown in the red region. (**d**) Normalized contribution ratio of pseudocapacitive at different scan rates. (**e**) GITT voltage profiles of SnS_2/RGO. (**f**,**g**) Discharge and charge reaction resistances. (**h**, **i**) The corresponding D_{Na} values in the first cycle.

The electrochemical performance of SnS_2/RGO as the anode material for PIBs was investigated using CR2016 half cells. Figure 6a exhibits the GCD profiles of SnS_2/RGO at 50 mA g^{-1}. The discharge/charge capacity of the first cycle is 983.1/520.8 mAh g^{-1}, respectively. The irreversible capacity is considered to be the formation of the SEI layer, which is a common phenomenon in transition metal-based anode materials [40]. In the following cycles, the profiles are well overlapped, which is coinciding with the CV results (Figure S7). In addition, it shows a high capacity of 520 mAh g^{-1} after 10 cycles. Figure 6b exhibits the rate performance of SnS_2/RGO. The reversible capacities of the SnS_2/RGO are 520.8, 405, 337.5, and 336.7 mAh g^{-1} mAh g^{-1} at 50, 100, 200 and 300 mA g^{-1}, respectively. Even at 500 mA g^{-1}, it still can remain a high capacity of 281.4 mAh g^{-1}, which indicates the excellent rate capability of SnS_2/RGO for K-ion storage. To further evaluate the cyclic stability of SnS_2/RGO electrode, the cycling test under current density of 100 and 300 mA g^{-1} are conducted. The SnS_2/RGO shows a high reversible capacity of 403.2 mAh g^{-1} at 100 mA g^{-1} after 80 cycles, with coulombic efficiency of almost 100% (Figure 6c). The long cycle performance of SnS_2/RGO electrode is shown in Figure 6d. It delivers a high reversible capacity of 130 mAh g^{-1} at 0.3 A g^{-1} after 300 cycles. The results

have been amply vindicated that the SnS_2/RGO electrode has excellent cycling stability for K-ion storage. To gain insight into the electrochemical kinetics of K-ion storage in SnS_2/RGO, we performed CV (0.2 to 1.0 mV s^{-1}) and GITT tests. As shown in Figure 6e–h and Figure S8, the large proportion of pseudocapacitive contribution, and high D values enables improvement of electrochemical performance, especially the rate capability. In addition, SnS_2/RGO also displays the excellent Li-ion storage performance (Figure S9). All in all, this hybrid structure demonstrates good electrode integrity, fast electrode reaction kinetics and the superior cycling stability, making SnS_2/RGO a great potential for the future electrochemical energy storage.
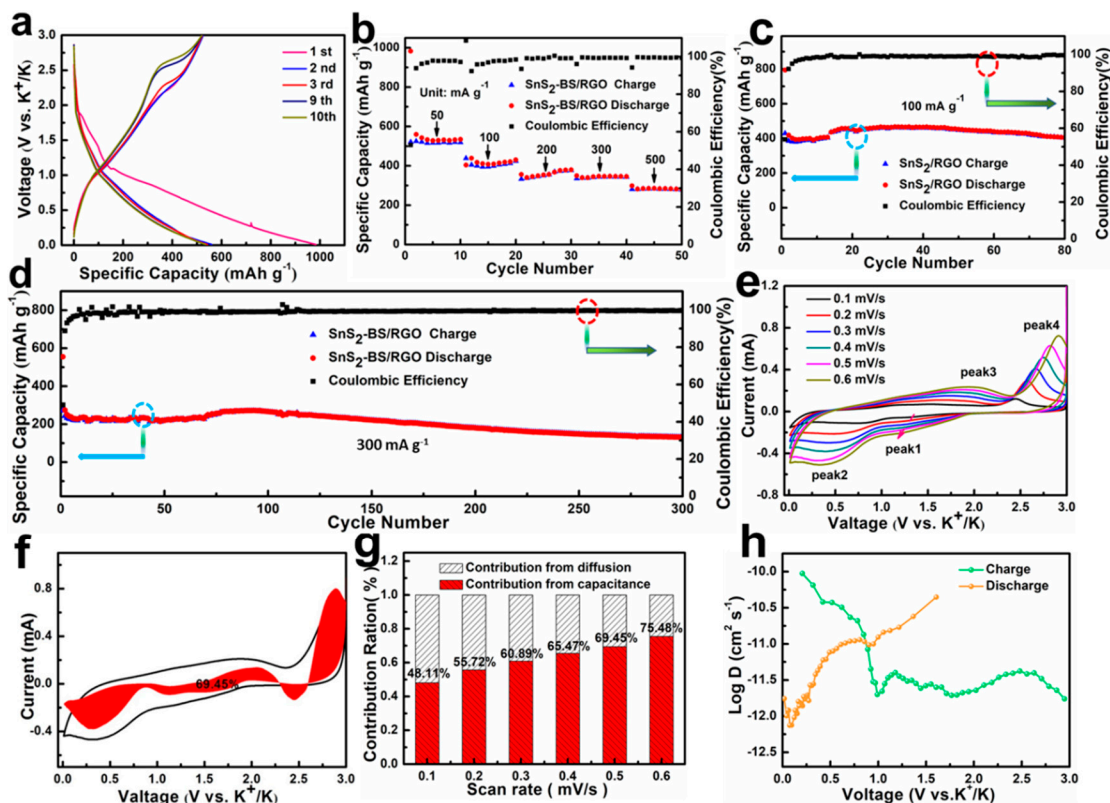

Figure 6. (**a**) Discharge/charge profiles of SnS_2/RGO at 50 mA g^{-1} in the potential range of 0.01–3.0 V vs. K/K$^+$. (**b**) Rate capability of SnS_2/RGO. (**c,d**) Cycling performance of SnS_2/RGO at 100 mA g^{-1} and 300 mA g^{-1}, respectively. (**e–g**) The kinetics and quantitative analysis of the K$^+$ storage behavior for SnS_2/RGO anodes. (**h**) Calculated diffusion coefficients during charging and discharging from SnS_2/RGO.

4. Conclusions

In summary, the well-designed sandwich-like hierarchical SnS_2/RGO structure have been synthesized via a facile solvothermal and subsequent annealing process. We found that 2-MIN can induce the growth of SnS_2 nanosheets on GO substrate during the solvothermal process, which has not been reported before. Benefiting from the good electrode integrity, excellent pseudocapacitive contribution and fast electrode reaction kinetics, SnS_2/RGO displays an outstanding rate performance (593 mAh g^{-1} at 0.2 A g^{-1} and 400 mAh g^{-1} at 2.0 A g^{-1}) and good cycling stability with a high capacity of 581 mAh g^{-1} at 0.5 A g^{-1} over 80 cycles when applied as anode for SIBs. Simultaneously, it delivers a high capacity of 130 mAh g^{-1} at 0.3 A g^{-1} after 300 cycles as anode for PIBs. These results indicate that the SnS_2/RGO is a promising anode material for electrochemical energy storage.

conditions. (a) In the presence of GO but without 2-MIN. (b) In the presence of 2-MIN but without GO. (c) In the absence of 2-MIN and GO, Figure S2: (a) FESEM image of SnS_2. (b) FESEM image of SnS_2 and the corresponding elemental mappings of Sn and S elements (as labeled), Figure S3: (a) Nitrogen adsorption-desorption curve of SnS_2/RGO, (b) the related pore size distribution curve, Figure S4: High resolution XPS spectrum of SnS_2, Figure S5: (a) Cyclic voltammetry (CV) curves of SnS_2/RGO. (b) FEEM image of SnS_2/RGO electrode after rate performance. (c) CV profiles of SnS_2 at different sweep rates. (d) Linear relationship of log (i) vs. log (v) plots at each redox peak. (e) CV curve with capacitive and diffusion-controlled contributions at 0.6 mV s^{-1}, in which the pseudocapacitive fraction is shown in the pink region, Figure S6: (a) Voltage versus time curve for one single GITT test. (b) The plots of voltage *vs.* root of pulse time ($\tau_{1/2}$), Figure S7: CV curves of the SnS_2/RGO electrode at a scan rate of 0.1 mV s^{-1} for the first four cycles for PIBs, Figure S8: (a) The charge/discharge curves of SnS_2/RGO electrode obtained during GITT measurement, (b) a single GITT titration curve during the charge process, and (c) the plots of voltage vs. root of pulse time ($\tau^{1/2}$), Figure S9: (a) The cycling performance of SnS_2/RGO at 0.6 A g^{-1}. (b) Rate performance of SnS_2/RGO electrode at various densities of 0.2–2.0 A g^{-1}, Table S1: Electrochemical performance comparisons of SnS_2/RGO electrode with those of the previously reported transition metal dichalcogenides anodes for SIBs.

Author Contributions: L.W.: conceptualized the idea, W.D., X.S. and Z.X.: supervised the work, H.S., C.Y., X.F. and L.H.: carried out the experiments, X.Z. and Y.Z.: contributed to the Raman study, C.D.: wrote the manuscript, F.J.: revised the manuscript. All authors have read and agree to the published version of the manuscript.

Conflicts of Interest: The authors declare that they have no conflict of interest.

References

1. Hamza, D.; Maziar, A.; Dana, A.; Zheng, Y.; Kamil, K.; Carlo, U.S.; Braja, K.M. MnO_2-Coated Dual Core-Shell Spindle-Like Nanorods for Improved Capacity Retention of Lithium-Sulfur Batteries. *ChemEngineering* **2020**, *4*, 42.
2. Zheng, Y.; Hamza, D.; Maziar, A.; Kamil, K.; Shankar, A.; Stoichko, A.; Bader, A.; Carlo, U.S.; Braja, K.M. Synthesis of a Very High Specific Surface Area Active Carbon and Its Electrical Double-Layer Capacitor Properties in Organic Electrolytes. *ChemEngineering* **2020**, *4*, 43.
3. Yang, C.; Lv, F.; Dong, K.; Lai, F.; Zhao, K.; Sun, F.; Dou, S.; Wang, Q.; Xu, J.; Zhang, P.; et al. Carbon-Coated Ultrathin Metallic V_5Se_8 Nanosheet for High-Energy-Density and Robust Potassium Storage. *Energy Storage Mater.* **2021**, *35*, 1–11. [CrossRef]
4. Li, W.; Wang, D.; Gong, Z.; Yin, Z.; Guo, X.; Liu, J.; Mao, C.; Zhang, Z.; Li, G. A Robust Strategy for Engineering Fe_7S_8/C Hybrid Nanocages Reinforced by Defect-Rich MoS_2 Nanosheets for Superior Potassium-Ion Storage. *ACS Nano* **2020**, *14*, 16046–16056. [CrossRef] [PubMed]
5. Dong, C.; Liang, J.; He, Y.; Li, C.; Chen, X.; Guo, L.; Tian, F.; Qian, Y.; Xu, L. $NiS_{1.03}$ Hollow Spheres and Cages as Superhigh Rate Capacity and Stable Anode Materials for Half/Full Sodium-Ion Batteries. *ACS Nano* **2018**, *12*, 8277–8287. [CrossRef]
6. Roy, K.; Li, T.; Ogale, S.; Robertson, N. Hybrid Perovskite-Like Iodobismuthates as Low-Cost and Stable Anode Materials for Lithium-Ion Battery Applications. *J. Mater. Chem. A* **2021**, *9*, 2689–2693. [CrossRef]
7. Zhang, Y.; Xie, M.; He, Y.; Zhang, Y.; Liu, L.; Hao, T.; Ma, Y.; Shi, Y.; Sun, Z.; Liu, N.; et al. Hybrid NiO/Co_3O_4 Nanoflowers as High-Performance Anode Materials for Lithium-Ion Batteries. *Chem. Eng. J.* **2021**, *420*, 130469. [CrossRef]
8. Shi, N.; Xi, B.; Huang, M.; Ma, X.; Li, H.; Feng, J.; Xiong, S. Hierarchical Octahedra Constructed by Cu_2S/MoS_2⊂Carbon Framework with Enhanced Sodium Storage. *Small* **2020**, *16*, 2000952. [CrossRef]
9. Zeng, T.B.; Chen, G.; Peng, Q.M.; Feng, D.; Wang, Q. Nano Sn_2S_3 Embedded in Nitrogenous-Carbon Compounds for Long-Life and High-Rate Cycling Sodium-Ion Batteries. *ChemSusChem* **2021**, *14*, 2383–2392. [CrossRef]
10. Ding, J.; Tang, C.; Zhu, G.; Sun, W.; Du, A.; He, F.; Wu, M.; Zhang, H. Integrating SnS_2 Quantum Dots with Nitrogen-Doped Ti_3C_2Tx MXene Nanosheets for Robust Sodium Storage Performance. *ACS Appl. Energy Mater.* **2021**, *4*, 846–854. [CrossRef]
11. Xiao, S.; Li, Z.; Liu, J.; Song, Y.; Li, T.; Xiang, Y.; Chen, J.S.; Yan, Q. Se-C Bonding Promoting Fast and Durable Na$^+$ Storage in Yolk-Shell $SnSe_2$@Se-C. *Small* **2020**, *16*, 2002486. [CrossRef] [PubMed]
12. Dong, C.F.; Guo, L.J.; He, Y.Y.; Chen, C.J.; Qian, Y.T.; Chen, Y.N.; Xu, L.Q. Sandwich-Like Ni_2P Nanoarray/Nitrogen-Doped Graphene Nanoarchitecture as a High-Performance Anode for Sodium and Lithium Ion Batteries. *Energy Storage Mater.* **2018**, *15*, 234–241. [CrossRef]
13. Li, D.; Dai, L.; Ren, X.; Ji, F.; Sun, Q.; Zhang, Y.; Ci, L. Foldable Potassium-Ion Batteries Enabled by Free-Standing and Flexible SnS_2@C Nanofibers. *Energy Environ. Sci.* **2021**, *14*, 424–436. [CrossRef]

14. Li, Y.F.; Wang, S.G.; Shi, Y.H.; Fan, C.Y.; Lin, J.; Wu, X.L.; Sun, H.Z.; Zhang, J.P.; Xie, H.M. In Situ Chemistry-Encapsulated Controlled SnS_2 Nanocrystal Composites for Durable Lithium/Sodium-Ion Batteries. *Dalton Trans.* **2020**, *49*, 15874–15882. [CrossRef]

15. Chen, G.; Li, X.; Zeng, T.; Han, R.; Wang, Q. Carbon-Coated Sn_2S_3 Hollow Spheres as High Performance Anode Materials for Sodium-Ion Batteries. *Carbon* **2021**, *171*, 464–473. [CrossRef]

16. Sun, Q.; Li, D.; Dai, L.; Liang, Z.; Ci, L. Structural Engineering of SnS_2 Encapsulated in Carbon Nanoboxes for High-Performance Sodium/Potassium-Ion Batteries Anodes. *Small* **2020**, *16*, e2005023. [CrossRef]

17. Zhao, B.; Song, D.; Ding, Y.; Li, W.; Wang, Z.; Jiang, Y.; Zhang, J. Size-Tunable SnS_2 Nanoparticles Assembled on Graphene as Anodes for High Performance Lithium/Sodium-Ion Batteries. *Electrochim. Acta* **2020**, *354*, 136730. [CrossRef]

18. Zhu, L.; Yang, X.X.; Xiang, Y.-H.; Kong, P.; Wu, X.W. Neurons-System-Like Structured SnS_2/CNTs Composite for High-Performance Sodium-Ion Battery anode. *Rare Met.* **2021**, *40*, 1383–1390. [CrossRef]

19. Wang, Y.; Zhou, J.; Wu, J.; Chen, F.; Li, P.; Han, N.; Huang, W.; Liu, Y.; Ye, H.; Zhao, F.; et al. Engineering SnS_2 Nanosheet Assemblies for Enhanced Electrochemical Lithium and Sodium Ion Storage. *J. Mater. Chem. A* **2017**, *5*, 25618–25624. [CrossRef]

20. Lakshmi, V.; Chen, Y.; Mikhaylov, A.A.; Medvedev, A.G.; Sultana, I.; Rahman, M.; Lev, O.; Prikhodchenko, P.V.; Glushenkov, A.M. Nanocrystalline SnS_2 Coated onto Reduced Graphene Oxide: Demonstrating the Feasibility of a Non-Graphitic Anode with sulfide chemistry for potassium-ion batteries. *Chem. Commun.* **2017**, *53*, 8272–8275. [CrossRef]

21. Yao, L.B.; Nie, M.; Zhu, C.Y.; Cai, R.; Xia, W.W.; Sun, L.T.; Xu, F. Revealing a Conversion-Alloying Reaction Mechanism Behind High Capacity and Rate Capability of SnS/N-Doped Graphene Anode by in Situ TEM. *Electrochim. Acta* **2019**, *297*, 46–54. [CrossRef]

22. Liu, Y.C.; Kang, H.Y.; Jiao, L.F.; Chen, C.C.; Cao, K.Z.; Wang, Y.J.; Yuan, H.T. Exfoliated-SnS_2 Restacked on Graphene as a High-Capacity, High-Rate, and Long-Cycle Life Anode for Sodium Ion Batteries. *Nanoscale* **2015**, *7*, 1325–1332. [CrossRef]

23. Li, S.; Zhao, Z.; Li, C.; Liu, Z.; Li, D. SnS2@C Hollow Nanospheres with Robust Structural Stability as High-Performance Anodes for Sodium Ion Batteries. *Nano-Micro Lett.* **2019**, *11*, 14. [CrossRef] [PubMed]

24. Sang, Z.; Yan, X.; Su, D.; Ji, H.; Wang, S.; Dou, S.X.; Liang, J. A Flexible Film with SnS_2 Nanoparticles Chemically Anchored on 3D-Graphene Framework for High Areal Density and High Rate Sodium Storage. *Small* **2020**, *16*, 2001265. [CrossRef] [PubMed]

25. Guan, S.; Wang, T.; Fu, X.; Fan, L.-Z.; Peng, Z. Coherent SnS_2/NiS_2 Hetero-Nanosheet Arrays with Fast Charge Transfer for Enhanced Sodium-Ion Storage. *Appl. Surf. Sci.* **2020**, *508*, 145241. [CrossRef]

26. Zhang, S.W.; Lv, W.; Qiu, D.; Cao, T.F.; Zhang, J.; Lin, Q.W.; Chen, X.R.; He, Y.B.; Kang, F.Y.; Yang, Q.H. An Ion-Conducting SnS-SnS_2 Hybrid Coating for Commercial Activated Carbons Enabling Their Use as High Performance Anodes for Sodium-Ion Batteries. *J. Mater. Chem. A* **2019**, *7*, 10761–10768. [CrossRef]

27. Cheng, L.; Zhang, Y.; Chu, P.; Wang, S.; Li, Y.; Ren, X.; Zhang, P.; Sun, L. Heterostructure Enhanced Sodium Storage Performance for SnS_2 in Hierarchical SnS_2/Co_3S_4 Nanosheet Array Composite. *J. Mater. Chem. A* **2021**, *9*, 1630–1642. [CrossRef]

28. Dong, C.F.; Guo, L.J.; Li, H.B.; Zhang, B.; Gao, X.; Tian, F.; Qian, Y.T.; Wang, D.B.; Xu, L.Q. Rational Fabrication of CoS_2/Co_4S_3@N-Doped Carbon Microspheres as Excellent Cycling Performance Anode for Half/Full Sodium Ion Batteries. *Energy Storage Mater* **2020**, *25*, 679–686. [CrossRef]

29. Zhang, Y.P.; Shen, Y.H.; Xie, X.B.; Du, W.; Kang, L.T.; Wang, Y.; Sun, X.Q.; Li, Z.H.; Wang, B. One-Step Synthesis of the Reduced Graphene Oxide@NiO Composites for Supercapacitor Electrodes by Electrode-Assisted Plasma Electrolysis. *Mater. Des.* **2020**, *196*, 109111. [CrossRef]

30. Zhou, Y.; Zhang, M.; Han, Q.; Liu, Y.; Wang, Y.; Sun, X.; Zhang, X.; Dong, C.; Jiang, F. Hierarchical 1T-MoS_2/MoOx@NC Microspheres as Advanced Anode Materials for Potassium/Sodium-Ion Batteries. *Chem. Eng. J.* **2021**, *428*, 131113. [CrossRef]

31. Wang, S.J.; Liu, S.S.; Li, X.M.; Li, C.; Zang, R.; Man, Z.M.; Wu, Y.H.; Li, P.X.; Wang, G.X. SnS_2/Sb_2S_3 Heterostructures Anchored on Reduced Grapheme Oxide Nanosheets with Superior Rate Capability for Sodium-Ion Batteries. *Chem. Eur. J.* **2018**, *24*, 3873–3881. [CrossRef]

32. He, Y.; Dong, C.; He, S.; Li, H.; Sun, X.; Cheng, Y.; Zhou, G.; Xu, L. Bimetallic Nickel Cobalt Sulfides with Hierarchical Coralliform Architecture for Ultrafast and Stable Na-Ion Storage. *Nano Res.* **2021**, 1–11. [CrossRef]

33. Wang, X.; Xi, B.J.; Ma, X.J.; Feng, Z.Y.; Jia, Y.X.; Feng, J.K.; Qian, Y.T.; Xiong, S.L. Boosting Zinc-Ion Storage Capability by Effectively Suppressing Vanadium Dissolution Dased on Robust Layered Barium Vanadate. *Nano Lett.* **2020**, *20*, 2899–2906. [CrossRef]

34. Dong, C.F.; Wu, L.Q.; He, Y.Y.; Zhou, Y.L.; Sun, X.P.; Du, W.; Sun, X.Q.; Xu, L.Q.; Jiang, F.Y. Willow-Leaf-Like ZnSe@N-Doped Carbon Nanoarchitecture as a Stable and High-Performance Anode Material for Sodium-Ion and Potassium-Ion Batteries. *Small* **2020**, *16*, 2004580. [CrossRef]

35. Wu, F.; Gao, X.; Xu, X.; Jiang, Y.; Gao, X.; Yin, R.; Shi, W.; Liu, W.; Lu, G.; Cao, X. MnO_2 Nanosheet-Assembled Hollow Polyhedron Grown on Carbon Cloth for Flexible Aqueous Zinc-Ion Batteries. *ChemSusChem* **2020**, *13*, 1537–1545. [CrossRef]

36. Guo, Q.; Shao, H.; Zhang, K.; Chen, G.; Kong, W.; Feng, X.; Gao, Y.; Liu, Y.; Wang, N.; Dong, C.; et al. CoP Nanoparticles Intertwined with Graphene Nanosheets as a Superior Anode for Half/Full Sodium-Ion Batteries. *ChemElectroChem* **2021**, *8*, 2022–2027. [CrossRef]

37. Cao, L.; Gao, X.; Zhang, B.; Ou, X.; Zhang, J.; Luo, W.-B. Bimetallic Sulfide Sb_2S_3@FeS_2 Hollow Nanorods as High-Performance Anode Materials for Sodium-Ion Batteries. *ACS Nano* **2020**, *14*, 3610–3620. [CrossRef]

38. Dong, C.; Zhou, Y.; Liu, W.; Du, W.; Zhang, X.; Sun, X.; Kang, L.; Zhang, X.; Jiang, F. Zn-Ce based Bimetallic Organic Frameworks Derived ZnSe/CeO$_2$ Nanoparticles Encapsulated by Reduced Graphene Oxide for Enhanced Sodium-Ion and Lithium-Ion Storage. *J. Alloy. Compd.* **2021**, *875*, 159903. [CrossRef]
39. Liu, X.; Hao, Y.; Shu, J.; Sari, H.M.K.; Lin, L.; Kou, H.; Li, J.; Liu, W.; Yan, B.; Li, D.; et al. Nitrogen/Sulfur Dual-Doping of Reduced Graphene Oxide Harvesting Hollow ZnSnS$_3$ Nano-Microcubes with Superior Sodium Storage. *Nano Energy* **2019**, *57*, 414–423. [CrossRef]
40. Zhao, Y.; Zhu, J.; Ong, S.J.H.; Yao, Q.; Shi, X.; Hou, K.; Xu, Z.J.; Guan, L. High-Rate and Ultralong Cycle-Life Potassium Ion Batteries Enabled by In Situ Engineering of Yolk-Shell FeS$_2$@C Structure on Graphene Matrix. *Adv. Energy Mater.* **2018**, *8*, 1802565. [CrossRef]